Paramagnetic NMR Shifts for Triplet Systems and Beyond with Modern Relativistic Density Functional Methods

Yannick J. Franzke*,[1] Florian Bruder*,[1] Sebastian Gillhuber,[2] Christof Holzer,[3] and Florian Weigend[1]

[1)] *Fachbereich Chemie, Philipps-Universität Marburg, Hans-Meerwein-Straße 4, 35032 Marburg, Germany*

[2)] *Institute of Inorganic Chemistry, Karlsruhe Institute of Technology (KIT), Engesserstraße 15, 76131 Karlsruhe, Germany*

[3)] *Institute of Theoretical Solid State Physics, Karlsruhe Institute of Technology (KIT), Wolfgang-Gaede-Straße 1, 76131 Karlsruhe, Germany*

(*Email for correspondence: florian.bruder@chemie.uni-marburg.de)

(*Email for correspondence: yannick.franzke@chemie.uni-marburg.de)

(Dated: 24 October 2023)

An efficient framework for the calculation of paramagnetic NMR (pNMR) shifts within exact two-component (X2C) theory and (current-dependent) density functional theory (DFT) up to the class of local hybrid functionals is presented. Generally, pNMR shifts for systems with more than one unpaired electron depend on the orbital shielding contribution and a temperature-dependent term. The latter includes the zero-field splitting, the hyperfine coupling, and the g-tensor. For consistency, we calculate these three tensors at the same level of theory, i.e. using scalar-relativistic X2C augmented with spin–orbit perturbation theory. Results for pNMR chemical shifts of transition-metal complexes reveal that this X2C-DFT framework can yield good results for both the shifts and the individual tensor contributions of metallocenes and related systems, especially if the hyperfine coupling (HFC) constant is large. For small HFC constants, the relative error is often large and sometimes the sign may be off. 4d and 5d complexes with more complicated structures demonstrate the limitations of a fully DFT-based approach. Additionally, a Co-based complex with very large zero-field splitting and pronounced multireference character is not well described. Here, a hybrid DFT-multireference framework is necessary for accurate results. Our results show that X2C is sufficient to describe relativistic effects and computationally cheaper than a fully relativistic approach. Thus, it allows to use large basis sets for converged hyperfine couplings. Overall, current-dependent meta-generalized gradient approximations (meta-GGAs) and local hybrid functionals show some potential, however, the currently available functionals leave a lot to be desired.

I. INTRODUCTION

Paramagnetic nuclear magnetic resonance (pNMR) and the related electron paramagnetic resonance (EPR) spectroscopy are widely used tools to characterize the spatial and electronic structure of systems with unpaired electrons.[1–4] Applications of pNMR cover a broad range including organometallic chemistry, biomolecular science, and materials science.[5–9]

The theoretical description of pNMR parameters is, however, considerably more involved than its closed-shell counter part.[10–24] In practice, most calculations construct the pNMR shielding tensor with the help of EPR parameters such as the hyperfine coupling tensor and the g-tensor. The latter are challenging properties for quantum chemistry themselves, as they necessitate a sophisticated treatment of electron correlation and relativistic effects together with large basis sets and an accurate molecular structure.

For a doublet system, the pNMR shielding tensor $\boldsymbol{\sigma}$ of a nucleus N in SI units reads[13]

$$\boldsymbol{\sigma}_N^{\mathrm{tot}} = \boldsymbol{\sigma}_N^{\mathrm{orb}} - \boldsymbol{\sigma}_N^{\mathrm{temp}} = \boldsymbol{\sigma}_N^{\mathrm{orb}} - \frac{10^6 h\mu_e}{g_N \mu_N} \frac{S(S+1)}{3k_B T} \boldsymbol{g} \cdot \boldsymbol{A}_N^{\mathrm{T}} \quad (1)$$

with the orbital shielding tensor $\boldsymbol{\sigma}^{\mathrm{orb}}$ (*Bm* convention for matrix rows and columns, B is the external magnetic field, m refers to the nuclear magnetic moment) and the temperature-dependent $\boldsymbol{\sigma}^{\mathrm{temp}}$ hyperfine shielding term. $\boldsymbol{\sigma}^{\mathrm{orb}}$ is the open-shell generalization from standard closed-shell NMR,[25] which can be obtained in a straightforward manner from it. The latter term depends on the EPR g-tensor $\boldsymbol{g}$ (*BS* convention) and the hyperfine coupling (HFC) tensor $\boldsymbol{A}$ in MHz (*mS* convention). g_N is the nuclear g-factor, μ_e and μ_N are the electron and nuclear magneton. h denotes Planck's constant, k_B Boltzmann's constant, T the temperature, and S the (effective) spin. For analysis, the hyperfine contribution is often partitioned into the Fermi-contact and pseudo-contact terms.[12,21,24,26] Typically, the paramagnetic shift is defined as the NMR chemical shift of an open-shell sample with respect to the closed-shell analog.

For systems with $S > 1/2$, the zero-field splitting (ZFS) tensor $\boldsymbol{D}$ needs to be considered. Based on the work of Soncini and Van den Heuvel the pNMR shielding tensor follows as[19]

$$\boldsymbol{\sigma}_N^{\mathrm{tot}} = \boldsymbol{\sigma}_N^{\mathrm{orb}} - \boldsymbol{\sigma}_N^{\mathrm{temp}} = \boldsymbol{\sigma}_N^{\mathrm{orb}} - \frac{10^6 h\mu_e}{g_N \mu_N k_B T} \boldsymbol{g} \cdot \boldsymbol{Z} \cdot \boldsymbol{A}_N^{\mathrm{T}} \quad (2)$$

with the (3×3) matrix[21]

$$Z_{kl} = \frac{1}{Q} \sum_{\lambda} e^{-\frac{E_\lambda}{k_B T}} \left[\sum_{a,a'} \left\langle S\lambda a \middle| \hat{S}_k \middle| S\lambda a' \right\rangle \left\langle S\lambda a' \middle| \hat{S}_l \middle| S\lambda a \right\rangle + 2k_B T \ \mathrm{Re} \sum_{\lambda' \neq \lambda} \sum_{a,a'} \frac{\langle S\lambda a | \hat{S}_k | S\lambda' a' \rangle \langle S\lambda' a' | \hat{S}_l | S\lambda a \rangle}{E_{\lambda'} - E_\lambda} \right] \quad (3)$$

including the eigenvalues E_λ of the ZFS Hamiltonian $\hat{\vec{S}} \cdot \boldsymbol{D} \cdot \hat{\vec{S}}$.

λ and a refer to the $(2S+1)$ eigenfunctions, i.e. a counts the components of degenerate states. Q is the partition function, i.e. $Q = \sum_{\lambda a} \exp[-E_\lambda/(k_B T)]$. This theoretical framework was first carried over to quantum-chemical methods by the groups of Autschbach[21,22] and Vaara.[23]

First, the Autschbach group used the zeroth-order regular approximation[26–29] (ZORA) with spin–orbit perturbation theory and density functional theory (DFT) for the computation of the orbital shielding, HFC, and g-tensors within the Amsterdam Density Functional (ADF) program.[30] While a first DFT based implementation of the ZFS tensor was originally implemented within ORCA,[31] it exhibited an insufficient agreement with experiment.[21] Experimentally determined ZFS tensors were therefore also used for the the determination of pNMR parameters in further studies.[21] Subsequently,[32] the workflow was adapted to also include ZORA-based approaches for the ZFS. The respective implementation in ADF supports the DFT ansätze of Pederson and Khanna,[33] Neese,[34] or Schmitt *et al.*,[35] excluding hybrid functionals and meta-generalized gradient approximations (meta-GGAs).[32,36] It however quickly came to attention that hybrid functionals are needed for an accurate description of NMR and EPR properties in many cases.[37–48]

Second, the Vaara group used DFT for the orbital and HFC tensors, while wavefunction-based multireference (MR) methods were chosen for the ZFS and g-tensor.[23,49] Later, this group applied scalar second-order Douglas–Kroll–Hess theory[50–52] for the ZFS and g-tensors with MR methods in ORCA,[31] whereas HFC tensors were obtained from four-component relativistic DFT with ReSpect,[45,53,54] c.f. refs. 49, 55–57. While this can lead to accurate results, it comes with a loss of methodological consistency. For instance, different relativistic Hamiltonians and basis sets are applied for the individual tensors. A fully consistent workflow treating all tensors on an equal footing is more desirable for many systems to allow for a straightforward analysis of the electronic structure and its connection to the obtained pNMR spectra. Further, both four-component approaches and MR methods are computationally demanding.

Recently, we presented efficient approaches for the calculation of ZFS,[58] HFC,[59,60] and g-tensors[60] within exact two-component (X2C) theory[61–71] and spin–orbit perturbation theory. The HFC and g-tensor can be further obtained at the self-consistent spin–orbit X2C level,[43,44,72] which results in an excellent agreement with the parent four-component Hamiltonian[43,44] and allowed us to rigorously assess the errors from the perturbative ansatz.[60] Compared to four-component approaches, X2C provides a substantial reduction of the computational costs. Based on this work and the respective orbital contribution,[73] all pNMR contributions can be evaluated in the same theoretical framework.

In this work, we extend the computational protocol for pNMR shifts in two distinct direction. First, we will demonstrate the applicability of the X2C framework for pNMR shifts. Second, we will consider modern density functional approximations up to the rung of local hybrid functionals[74] (LHFs) and meta-GGAs incorporating the paramagnetic current density.[75–77] The latter is needed to properly generalize the kinetic-energy density τ of meta-GGAs and LHFs for EPR and NMR properties.[41,58,72,78–82] In the absence of magnetic perturbations, τ is defined as

$$\tau^\sigma = \frac{1}{2}\sum_i |\hat{\vec{p}}\ \varphi_i^\sigma|^2 = \frac{1}{2}\sum_i \left(\hat{\vec{p}}\varphi_i^\sigma\right)^\dagger \cdot \left(\hat{\vec{p}}\varphi_i^\sigma\right) \tag{4}$$

with the momentum operator $\hat{\vec{p}}$ and the Kohn–Sham spin orbitals φ_i^σ. This variable is formally used to identify inhomogenities in the electron density and is a key ingredient of modern functionals with accurate thermochemical properties.[83–86] For magnetic properties, τ needs to be generalized to

$$\tilde{\tau}^\sigma = \tau^\sigma - \frac{|\vec{j}_p^\sigma|^2}{2\rho^\sigma} \tag{5}$$

with the paramagnetic current density[87]

$$\vec{j}_p^\sigma = -\frac{\mathrm{i}}{2}\sum_i \left(\varphi_i^{\sigma,*}\vec{\nabla}\varphi_i^\sigma - \varphi_i^\sigma\vec{\nabla}\varphi_i^{\sigma,*}\right) = \mathrm{Re}\sum_i \left(\varphi_i^{\sigma,*}\ \hat{\vec{p}}\ \varphi_i^\sigma\right) \tag{6}$$

to satisfy fundamental theoretical constraints such as gauge invariance and the von-Weizsäcker inequality.[88] Overall, a consistent and highly efficient framework is formed. The accuracy and limitations of such a fully DFT-based framework will be critically assessed. To do so, we will first consider the well known 3d metallocenes and then move on to more complicated 3d, 4d, and 5d complexes.

II. COMPUTATIONAL METHODS

First, we study the ^{1}H and ^{13}C shifts of nickelocene (Cp_2Ni, Cp = cyclopentadienyl) with $S = 1$ at 298 K. The structure was optimized with the BP86 functional[89,90] (grid size 3a[91–93]) and the D4 dispersion correction[94] using the X2C Hamiltonian[95,96] in the diagonal local approximation to the unitary transformation[97] (DLU) and the x2c-QZVPall-s basis set.[98] The finite nucleus model based on a Gaussian charge distribution[99] is applied for the scalar potential and the vector potential. Note that the resolution of the identity approximation (RI-J) is used in conjunction with tailored auxiliary basis sets[98,100] throughout this work, as this leads to substantial speedups and only introduces very small errors.[101] The subsequent pNMR calculations are performed with the generalized gradient approximation (GGA) functionals BP86,[89,90] KT2,[102] KT3,[103] and PBE,[104] the GGA-based hybrids PBE0,[104,105] BH&HLYP,[89,106,107] B3LYP (VWN V-fit),[89,106,108] CAM-B3LYP,[109] CAM-QPT-00,[110] CAM-QPT-01,[110] CAM-QTP-02,[111] HSE06,[112–114] LC-ωPBE,[115] and ωB97X-D,[116] as well as the pure and hybrid meta-GGAs TPSS,[117] TPSSh,[117,118] TPSS0,[117,119] r^{2}SCAN,[120,121] r^{2}SCANh,[120–122] r^{2}SCAN0,[120–122] r^{2}SCAN50,[120–122] Tao–Mo,[123] M06-L,[124] M11-L,[125] MN12-L,[126] MN15-L,[127] MN15,[128] PKZB,[129] BMK,[130] B97M,[131] ωB97M,[132] and TASK.[133] Local hybrids are represented by the LH12ct-SsirPW92 (LH12ct),[134] LH12ct-SsifPW92,[134] LH20t,[135] LH20t-noCF (LH20t neglecting the calibration

function),[135] TMHF,[136] TMHF-3P,[136] LHJ-HF,[136] LHJ-HFcal,[136] LHJ14,[137] mPSTS-noa2,[41,138] and mPSTS-a1[41,138] functionals. Additionally, unrestricted Hartree–Fock (HF) theory was applied. LibXC[139–141] was used for all functionals except BP86, BH&HLYP, B3LYP, PBE, PBE0, TPSS, TPSSh, and the local hybrids. The conductor-like screening model[101,142] (COSMO) is applied for the solvent toluene (permittivity 2.4, refractive index 1.4969). Inclusion of the paramagnetic current density[41,58,78,80] is indicated below by the prefix "c". Note that we apply the seminumerical approximation for the left-hand side of the response equations for global and range-separated hybrids (grid size −1).[41,143] LHFs apply the seminumerical scheme throughout.[41,143–146] Ground-state self-consistent field (SCF) energies are converged up to $10^{-8}\,E_h$ and linear response equations are converged with a threshold of 10^{-7} for the norm of the residuum.[147,148] The ZFS, HFC, and g-tensors are computed with the DLU-X2C approach and the modified screened nuclear spin–orbit (mSNSO) approximation[149–151] for the spin–orbit perturbation,[58–60] while the orbital contribution is obtained with scalar DLU-X2C.[73] These calculations are performed with the mpshift module[43,44,58–60,73,101,152,153] of TURBOMOLE[154–157] and the tensors are stored on disk for the PNMRShift program.[21,26,158] Gauge-including atomic orbitals are employed[159,160] for the g-tensor and the orbital shielding. Paramagnetic NMR shifts are calculated relative to ferrocene, see Supporting Information for detailed results. The sign convention of refs. 161,162 is chosen. Additional results with tetramethylsilane (TMS) serving as reference for the NMR shifts are available in the Supporting Information.

Second, this protocol is applied to the ^{1}H and ^{13}C shifts of vanadocene ($S = 3/2$, 298 K), chromocene ($S = 1$, 298 K), manganocene ($S = 5/2$, 390 K), and cobaltocene ($S = 1/2$, 298 K). Based on the results for nickelocene, only the functionals BP86,[89,90] KT3,[103] PBE,[104] PBE0,[104,105] HSE06,[112–114] LC-ωPBE,[115] ωB97X-D,[116] B3LYP (VWN V-fit),[89,106,108] CAM-B3LYP,[109] BH&HLYP,[89,106,107] PKZB,[129] TPSS,[117] TPSSh,[117,118] r^{2}SCAN,[120,121] and LH20t[135] are considered. It is noted that the EPR properties and thus the pNMR shifts are not substantially affected by the specific conformer for vanadocene, i.e. eclipsed vs. staggered.[163] We have verified that this also holds at the level of theory in the present work for all metallocenes. For simplicity and in agreement with refs. 23,32,55, we consider the eclipsed structure.

Third, the quinolyl-functionalized cyclopentadienyl Cr(III) complex ($S = 3/2$, 298 K) studied previously by the Vaara group is revisited.[15,23] In ref. 23, DFT (PBE0) was applied for the orbital shielding and the hyperfine coupling, while the complete active space self-consistent field (CASSCF) and *n*-electron valence state perturbation theory of second-order (NEVPT2) MR methods were used for the g-tensor and the ZFS. The structure optimized at the B3LYP/def2-TZVP level[89,106,108,164] is directly taken from ref. 23. For comparison, this work follows the same notation. Solvent effects as present in the experiment[165] are accounted for by the COSMO model, using the settings for chloroform (permittivity 4.8, refractive index 1.4458). The same set of functionals, and basis sets as for the general metallocene study is applied. For this study, the structure of the NMR reference TMS was optimized at the BP86-D4/DLU-X2C/x2c-TZVPall-s level of theory using the COSMO settings for chloroform.

Fourth, the shifts of the Mo(III) complex Mo[N(R)Ar]$_3$ (R = C(CD$_3$)$_2$CH$_3$, Ar = 3,5-C$_6$H$_3$Me$_2$, Me = methyl) with $S = 3/2$ are studied.[166] Given the enlarged size of this complex, the computational workflow was slightly adapted for efficiency. The molecular structure was optimized with BP86-D4/DLU-X2C[89,90,94–96] and the x2c-SVPall basis set.[100] COSMO settings for benzene are applied (permittivity 2.28, refractive index 1.501). For consistency, the structure of TMS, serving as the NMR reference, was also optimized at this level. NMR shieldings and shifts (298 K) are obtained with the x2c-QZVPall-s basis set[98] and the same functionals as above. Note that isotope effects are neglected, and thus the deuterated substituent R becomes identical to tBu = C(CH$_3$)$_3$.

Fifth, the Co(II) pyrazolylborate complex HPYBCO with $S = 3/2$ at 298 K is investigated. It was shown that DFT methods (PBE, PBE0) fail for the ZFS and g-tensor of this complex.[23,49] We confirmed this failure with the broader range of functionals listed above. Thus, a modified version of the protocol for the Cr(III) complex is suggested as follows. The ZFS and g-tensor are calculated with strongly-contracted (SC) NEVPT2 as implemented in ORCA.[167,168] The DKH2 Hamiltonian[50–52] is used in conjunction with a finite nucleus model and the x2c-type basis sets.[100] For the latter, earlier work has shown that these can also be used with low-order DKH.[98] Here, the x2c-TZVPall basis is used for Co and its neighbors, while the x2c-SVPall basis is employed for the other atoms to reduce the computational demands. The x2c-universal auxiliary basis set[98,100] is used for the RI approximation to the spin–spin coupling contribution to the ZFS tensor. The active space (seven metal d-electrons in five 3d orbitals) is chosen identically to previous studies by the Vaara group.[23,49] All 40 doublet and 10 quartet states of the CAS(7,5) ansatz were included in a state averaged approach. Remaining computational settings are chosen to be the same as for the Cr(III) complex. The molecular structure was taken from ref. 49.

Finally, calculated shifts for the complexes Cp*MoCl$_3$(PMePh$_2$) with $S = 1$ and ReCl$_3$py$_2$(PPh$_3$) with $S = 1$ (Cp* = 1,2,3,4,5-pentamethylcyclopentadienyl, Ph = phenyl, py = pyridine = NC$_5$H$_6$) are compared with experimental data at 298 K.[169,170] Structures for these complexes were optimized at the BP86-D4 level[89,90,94] using the x2c-TZVPall-s basis set.[93] Solvent effects are accounted for by the COSMO model using the settings for acetone (permittivity 21.01, refractive index 1.3588, Mo complex) and chloroform (permittivity 4.8, refractive index 1.4458, Re complex). For consistency, the structure of the NMR reference TMS was also optimized at the respective level of theory. Paramagnetic shifts were computed with the x2c-QZVPall-s basis[98] and the BP86[89,90] PBE,[104] PBE0,[104,105] B3LYP (VWN V-fit),[89,106,108] CAM-B3LYP,[109] ωB97X-D,[116] and cTPSSh[117,118] functionals. Other computational settings such as the thresholds, grids for the DFT part or the seminumerical exchange approximation for the CPKS are unchanged. In addition to the full DFT framework, ZFS and g-tensors for both complexes were calculated within the CASSCF/NEVPT2

framework in a similar fashion as in ref. 49 with ORCA.[167,168] The SC-NEVPT2 approach was chosen. Scalar-relativistic effects were included within the DKH2 Hamiltonian[50–52] and a finite Gaussian nucleus model[99] was employed. The calculation of both the ZFS and the g-tensor was done with the effective Hamiltonian approach within ORCA.[167] For $\mathbf{Cp^*MoCl_3}(\mathbf{P}MePh_2)$, the active space contained the two metal d-electrons in the five 4d orbitals of the Mo atom. All 15 singlet and 10 triplet states of the CAS(2,5) ansatz were included in a state averaged approach. The x2c-TZVPall basis was chosen for the central metal atom and the atoms in the first coordination sphere, marked in bold font. In the Cp^* ring, only the C atoms forming the ring were described with the x2c-TZVPall basis. The smaller x2c-SVPall basis was chosen for the remaining atoms. The x2c-universal auxiliary basis set[98,100] was used for the RI approximation to the spin–spin coupling contribution to the ZFS tensor. For $\mathbf{ReCl_3}(\mathbf{N}C_5H_6)_2(\mathbf{P}Ph_3)$, the active space contained the four metal d-electrons in the five 5d orbitals of the Re atom. All 50 singlet, 45 triplet, and 5 quintet states of the CAS(4,5) ansatz were included in a state averaged approach. The x2c-TZVPall basis was used for the Re, the three Cl, the P and the two N atoms, again marked in bold font.

III. RESULTS AND DISCUSSION

A. Nickelocene

Nickelocene serves as the archetype for pNMR shifts and was previously studied with various methods,[14,21,23] as experimental results, showing a pronounced impact of the hyperfine terms, are available.[162,171–174] To begin with, we check if multireference methods such as CASSCF or NEVPT2 are required for the ZFS and g-tensor. Results for these EPR parameters are listed in Tab. I. Here, the first attempts for the ZFS with DFT by Martin and Autschbach did not yield accurate results.[21] In contrast, the results herein are in very good agreement with the experimental findings and confirm our previous studies in ref. 58. Note that we use a different approach for the ZFS than previous work by other authors, i.e. we use a generalization[58] of the formalism by Schmitt *et al.*,[35] while Martin and Autschbach[21] originally applied that of Neese[34,175,176] and found D = 1.62 cm^{-1} with PBE0. The good agreement for the ZFS in the present work allows us to use the computationally determined ZFS tensor instead of the experimental one as initially done by Martin and Autschbach. Further, multireference methods are not not needed.

Results for the paramagnetic NMR shifts are shown in Tab. II. Due to the comparably large HFC constant, the contribution from the Fermi-contact term dominates the total shift, as shown in the Supporting Information. We note in passing that the ZFS contribution changes the ^{1}H and ^{13}C shift of BH&HLYP by 0.5 and 60 ppm (see Supporting Information Metallocenes.xlsx). Overall, hybrid functionals outperform pure semilocal approximations. PBE0, cr^{2}SCAN50, and HSE06 perform best for the ^{1}H shift followed by cTPSSh, ωB97X-D, and cTPSS. Especially for PBE0, the results presented herein are an improvement upon the results listed in ref. 32. The r^{2}SCAN family performs reasonably well for the ZFS and g-tensor, however, the paramagnetic NMR shift is severely overestimated for all functionals except cr^{2}SCAN50, which showed the largest deviations towards the experimental EPR data among this family. Therefore, the good performance of cr^{2}SCAN50 for the shifts is at least partly due to favorable error cancellation. Also, the Minnesota functionals are not well suited for paramagnetic NMR shifts. We note that these functional families may show slow convergence or grid instabilities.[177–179]

TABLE I. EPR properties of nickelocene with selected density functionals. Isotropic hyperfine coupling constant A in MHz, isotropic g value g_{iso}, and ZFS D parameter in cm^{-1}. See Supporting Information (EPR sheet in Metallocenes.xlsx) for results with all functionals. The ZFS E parameter vanishes for metallocenes such as nickelocene. Experimental findings (Expt.) for the solid state are taken from ref. 171. Other measurements found a D value of 31.6 or 33.6 cm^{-1}.[172,173] CASSCF and NEVPT2 results with the def2-TZVP basis set are taken from ref. 23, which use a molecular structure obtained from B3LYP/def2-TZVP.

Functional	A(^{1}H)	A(^{13}C)	g_{iso}	D
KT3	−5.218	4.615	2.025	17.11
BP86	−4.210	3.932	2.024	19.70
B3LYP	−3.653	5.564	2.043	25.08
CAM-B3LYP	−3.535	5.679	2.047	26.30
BH&HLYP	−3.046	6.335	2.086	40.71
PBE	−3.943	4.377	2.024	20.16
PBE0	−3.586	5.404	2.049	26.79
HSE06	−3.629	5.271	2.048	26.61
LC-ωPBE	−3.879	5.131	2.039	23.01
ωB97X-D	−3.497	6.213	2.049	27.70
cPKZB	−4.906	4.711	2.025	19.47
cTPSS	−3.868	5.228	2.025	18.91
cTPSSh	−3.770	5.543	2.042	21.12
cωB97M	−2.525	3.429	2.050	30.60
cr^{2}SCAN	−4.990	8.039	2.033	23.74
cr^{2}SCANh	−4.725	7.951	2.043	27.58
cr^{2}SCAN0	−4.264	7.739	2.059	34.77
cr^{2}SCAN50	−3.479	7.184	2.096	50.23
cLH12ct	−3.319	3.146	2.048	31.20
cLH20t	−3.090	5.186	2.045	26.92
Expt. (Solid State)	–	–	2.04	25.6
CASSCF	–	–	2.253	70.1
NEVPT2	–	–	2.125	40.1

Local hybrid functionals such as LH12ct and LH20t show some potential, however, LHFs are no systematic improvement over conventional global and range-separated hybrids. As shown by results in the Supporting Information, the calibration function (c.f. LH20t vs. LH20t-noCF and LHJ-HFcal vs. LHJ-HF) does not substantially affect the EPR properties and consequently the paramagnetic shift is also not notably altered.

The total wall time for the complete pNMR shift calculation (including the preceding SCF procedure) is less than one hour with conventional hybrids (12 OpenMP threads of an Intel Xeon Gold 6212U CPU at 2.40 GHz). LHF calculations

TABLE II. ^{1}H paramagnetic NMR shifts δ^{para} (shift relative to ferrocen) of nickelocene ($S = 1$) with selected density functional approximations at 298 K. Shifts are given in ppm. See Supporting Information (pNMR sheet Metallocenes.xlsx) for results with all functionals and the respective ^{13}C shifts. Experimental data (Expt.) is taken from ref. 162. Note that a small orbital contribution is obtained in the computational studies.

Functional	Orbital	FC	PC	Total
KT3	−1.35	372.75	0.02	371.42
BP86	−1.37	300.56	0.11	299.30
B3LYP	−1.33	263.24	0.26	262.17
CAM-B3LYP	−1.30	255.24	0.27	254.21
BH&HLYP	−1.32	224.13	1.03	223.85
PBE	−1.38	281.59	0.13	280.34
PBE0	−1.35	259.18	0.44	258.27
HSE06	−1.35	262.24	0.44	261.33
LC-ωPBE	−1.31	278.99	0.17	277.85
ωB97X-D	−1.30	252.78	0.21	251.69
cPKZB	−1.40	350.51	0.19	349.30
cTPSS	−1.33	276.27	0.05	274.99
cTPSSh	−1.32	270.38	0.14	269.20
cωB97M	−1.29	182.63	0.14	181.47
cr^{2}SCAN	−1.41	357.93	0.32	356.85
cr^{2}SCANh	−1.40	340.41	0.45	339.47
cr^{2}SCAN0	−1.40	309.56	0.73	308.88
cr^{2}SCAN50	−1.51	256.97	1.43	256.89
LH12ct	−1.26	235.89	0.24	234.88
cLH20t	−1.20	222.91	0.16	221.86
Expt. (Toluene)				257.44

take about 1.5–2 hours. Therefore, the X2C-DFT framework only requires widely available low-cost computer hardware.

B. Vanadocene, Chromocene, Manganocene, and Cobaltocene

Based on the results for nickelocene, we consider a subset of the density functional approximations for the other metallocenes. The ^{1}H paramagnetic shifts for vanadocene ($S = 3/2$, 298 K), chromocene ($S = 1$, 298 K), manganocene ($S = 5/2$, 390 K), and cobaltocene ($S = 1/2$, 298 K) are listed in Tab. III. Based on the EPR results for nickelocene in Sec. III A and previous studies,[32,55] multireference methods are not needed for these metallocenes as well.

DFT performs very well for chromocene and cobaltocene. Here, most functionals yield results close to the experiment.[161,162] Especially, the PBE-based hybrids and ωB97X-D perform excellently. Also, the local hybrid LH20t reproduces the experimental shift up to 12 and 5 ppm. Compared to nickelocene, the ZFS parameter D is small for chromocene with a range of -1 to $-4\,\text{cm}^{-1}$. The experimental result[180] is $-15.1\,\text{cm}^{-1}$ and previous CASSCF/NEVPT2 studies found a D value of about $-10\,\text{cm}^{-1}$.[23] Neglecting the ZFS contribution for chromocene at the PBE0 level changes the shift by less than 0.1 ppm. Thus, the paramagnetic shift is completely determined by the hyperfine coupling tensor, which is dominated by the Fermi-contact term and hence the spin-excess density at the respective nucleus.

TABLE III. ^{1}H paramagnetic NMR shifts δ^{para} (shift relative to ferrocene) of vanadocene ($S = 3/2$, 298 K), chromocene ($S = 1$, 298 K), manganocene ($S = 5/2$, 390 K), and cobaltocene ($S = 1/2$, 298 K) with selected density functional approximations at 298 K. Shifts are given in ppm. See Supporting Information (pNMR sheet in Metallocenes.xlsx) for the complete separation of the shifts into the orbital, Fermi-contact (FC), and pseudo-contact (PC) contributions. Therein, we also list the EPR results (EPR sheet in Metallocenes.xlsx). Experimental data (Expt.) in solution (toluene) are taken from refs. 161,162.

Functional	Cp_2V	Cp_2Cr	Cp_2Mn	Cp_2Co
KT3	−432.97	−415.39	47.18	81.46
BP86	−392.17	−367.39	13.70	74.81
B3LYP	−381.39	−338.36	11.68	55.24
CAM-B3LYP	−373.03	−320.78	14.99	53.63
BH&HLYP	−349.47	−302.10	21.27	38.20
PBE	−392.81	−364.57	4.33	70.86
PBE0	−369.51	−335.98	8.97	50.14
HSE06	−370.39	−336.47	8.23	51.02
LC-ωPBE	−368.29	−319.89	19.55	63.16
ωB97X-D	−364.74	−307.92	27.00	55.80
cPKZB	−398.53	−378.16	40.60	87.00
cTPSS	−390.29	−363.52	16.13	62.69
cTPSSh	−380.82	−350.77	17.93	55.15
r^{2}SCAN	−393.30	−379.55	75.56	81.50
cLH20t	−338.75	−304.10	8.84	49.41
Expt. (Toluene)	−314.58	−316.52	−23.30	54.80

For vanadocene, the given density functional approximations perform reasonably well but larger deviations are observed. BH&HLYP and cLH20t perform best and show deviations of 35 ppm and 24 ppm, respectively. Again, the shift is almost completely determined by the Fermi-contact term. As this term is sensitive towards the basis set, we checked if an even larger basis than QZVP can improve the results. Decontracting the basis set for hydrogen and carbon does not notably change the results (see the file Metallocenes.xlsx of the Supporting Information). This shows that the segmented-contracted x2c-QZVPall-s basis set is already sufficient for vanadocene and there is no need for decontracting this basis set.

The shift of manganocene shows the wrong sign, which is due to the hyperfine coupling tensor. This was already observed by Martin and Autschbach with the ZORA approach and Slater-type basis functions.[32] To study the origin of the incorrect sign, we also tried other settings. First, the Hamiltonian was changed to the self-consistent spin–orbit X2C level.[43] However, this did not result in notably different results for the hyperfine coupling (isotropic constant -0.029 MHz vs. -0.027 MHz). Thus, spin–orbit perturbation theory is clearly sufficient. Second, we again checked the basis set convergence by decontracting the x2c-QZVPall-s basis for H and C (x2c-QZVPall-unc).[43,98] This changes the isotropic HFC with PBE from -0.029 MHz to -0.044 MHz, which alters the shielding constant by 3.5 ppm. For completeness, we also

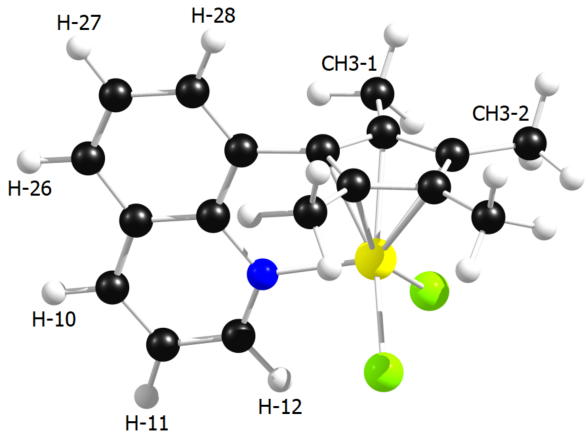

FIG. 1. Molecular structure of the quinolyl-functionalized cyclopentadienyl Cr(III) complex with $S = 3/2$ and labels for the ^{1}H NMR. Color code: hydrogen white, carbon black, nitrogen blue, chlorine green, chromoium yellow. See also ref. 23 for details on the structure optimization.

considered other basis sets, which are frequetly used for NMR studies. Application of the x2c-TZVPall-s basis set[93] results in -0.073 MHz, while the fully decontracted cc-pVTZ basis for all atoms[181,182] leads to -0.039 MHz. Further using the contracted or decontracted IGLO-III bases for hydrogen and carbon[183] does not change the sign, however, the HFC constant is almost zero with the contracted IGLO-III basis. Additionally, the Sapporo-TZP-2012 basis set[184] yields similar results as the x2c-type bases. The fully decontracted dyall-vdz, dyall-vtz, and dyall-vqz basis sets[185] taken from the Dirac program[186,187] are employed. This leads to HFC constants of -0.046 MHz, -0.045 MHz, and -0.048 MHz, respectively. Finally, very similar results are obtained with the NMR/EPR-tailored pcSseg-4 basis[188] for Mn and pcH-4 for C and H.[189] So, none of the considered basis sets leads to results reproducing the experimental finding and we can attribute the insufficient results to the density functional approximations for the hyperfine coupling, as also MR methods for the ZFS and g-tensor together with DFT for the HFC do not result in an accurate description of the experiment.[55]

To sum up, X2C-DFT can also perform well for metallocenes other than nickelocene. Hybrid functionals are pivotal for accurate results. Compounds such as manganocene with a small hyperfine coupling constant are challenging, as the sign of the Fermi-contact term may be incorrect and consequently the paramagnetic shift inherits this error. In line with previous studies on vanadocene and manganocene, the ZFS tensor is of minor importance for the paramagnetic shift at the given temperatures.[32] Thus, an accurate description of the hyperfine coupling tensor is the decisive part for metallocenes and multireference methods for the ZFS and g-tensors are not needed.

TABLE IV. EPR properties of the quinolyl-functionalized cyclopentadienyl Cr(III) complex at the DFT/DLU-X2C/x2c-QZVPall-s level of theory. CASSCF and NEVPT2 results with a locally dense def2-TZVP/def2-SVP basis set are taken from ref. 23. The ZFS parameter D is given in cm^{-1}. g_{iso} denotes the isotropic g factor, while g_{11}, g_{22}, and g_{33} refer to the eigenvalues, i.e. the principal components.

Functional	g_{iso}	g_{11}	g_{22}	g_{33}	D	E/D
KT3	1.996	1.992	1.995	2.000	1.78	0.013
BP86	1.996	1.992	1.995	2.001	1.88	0.002
B3LYP	1.992	1.987	1.991	1.998	2.28	0.019
CAM-B3LYP	1.991	1.985	1.990	1.998	2.36	0.022
BH&HLYP	1.986	1.979	1.984	1.994	2.58	0.037
PBE	1.996	1.992	1.995	2.001	1.91	0.001
PBE0	1.991	1.985	1.990	1.998	2.27	0.032
HSE06	1.991	1.985	1.990	1.998	2.28	0.030
LC-ωPBE	1.992	1.987	1.990	1.998	2.22	0.052
ωB97X-D	1.990	1.984	1.989	1.997	2.54	0.019
cPKZB	1.996	1.991	1.995	2.000	1.82	0.009
cTPSS	1.996	1.992	1.995	2.001	1.84	0.001
cTPSSh	1.994	1.990	1.993	1.999	1.98	0.013
cr^{2}SCAN	1.994	1.990	1.993	1.999	1.71	0.021
cLH20t	1.991	1.985	1.990	1.998	2.47	0.023
CASSCF	1.958	1.944	1.952	1.979	2.97	0.047
NEVPT2	1.970	1.959	1.966	1.985	2.85	0.032

C. Quinolyl-Functionalized Cyclopentadienyl Cr(III) Complex

The Cr(III) complex shown in Fig. 1 was previously studied by Vaara *et al.* with a hybrid DFT/MR approach.[23] The g-tensor and ZFS parameters were obtained with CASSCF and NEVPT2, while PBE0 was used for the HFC and orbital shielding. Thus, we first compare the g-tensor and ZFS with X2C-DFT to the CASSCF and NEVPT2 results in Tab.IV to check whether multireference methods are required. Note that the CASSCF and NEVPT2 calculations were performed without including scalar relativistic effects and using smaller basis sets than in our DFT methods. All functionals yield a very similar isotropic g-factor of about 1.99, while CASSCF and NEVPT2 lead to 1.958 and 1.970. Here, the deviation between CASSCF and NEVPT2 is somewhat smaller than the deviation between DFT and NEVPT2. Similar findings hold for the ZFS parameter D. Here, most hybrid functionals lead to a deviation of about 0.4 cm^{-1} from the NEVPT2 results. Overall, the differences for the g and ZFS tensor between all methods are comparably small and almost insignificant for the pNMR shifts. Thus, multireference methods are not needed for this Cr(III) complex.

The NMR chemical shifts relative to TMS are listed in Tab. V. Here, the previous attempt with PBE0/NEVPT2 and the def2-TZVP basis results in an excellent agreement with the experiment for H-11. A good agreement is observed for H-10, H-12, or H-27. The deviations amount to less than 20%. Somewhat larger differences are found for H-26 and the CH_3-2 group. Still, the sign of the shift is reproduced correctly. For the CH_3-1 group, this does not hold. Here, a large discrepancy is found, i.e. calculations lead to -12 ppm which is not in agreement with the experimental shift of 27.6 ppm. Our

TABLE V. ^{1}H NMR shift (in ppm) of the quinolyl-functionalized cyclopentadienyl Cr(III) complex ($S = 3/2$, 298 K) at the DFT/DLU-X2C/x2c-QZVPall-s level of theory. Note that we use the notation of ref. 23 for the position of the hydrogens, see also Fig. 1. Additionally, PBE0/NEVPT2 results by Vaara *et al.* are taken from ref. 23. Here, the PBE0/def2-TZVP method is used for the hyperfine coupling tensor and the orbital shielding, while NEVPT2 with a locally dense def2-TZVP/def2-SVP basis is applied for the g-tensor and the zero-field splitting. Shifts are given relative to tetramethylsilane, see Supporting Information (pNMR sheet in Cr-Complex.xlsx). Experimental data (Expt.) are taken from ref. 165. Additional results with B3LYP and the superseded formalism of Pennanen and Vaara[14] are taken from ref. 15.

Functional	H-10	H-11	H-12	H-26	H-27	H-28	CH_3-1	CH_3-2
KT3	−107.1	58.8	−162.9	−43.8	13.2	−7.4	−31.6	−114.7
BP86	−101.0	59.8	−134.0	−33.5	13.6	−8.5	22.6	−55.2
B3LYP	−59.8	48.8	−85.4	−25.1	17.2	−5.7	−8.3	−76.4
CAM-B3LYP	−58.9	53.1	−82.1	−27.4	24.9	−10.6	−13.6	−79.3
BH&HLYP	−74.8	68.4	−96.9	−41.9	39.5	−23.8	−21.9	−84.0
PBE	−93.6	56.1	−121.4	−31.5	11.8	−7.9	26.4	−48.0
PBE0	−67.0	52.0	−105.4	−32.0	22.2	−8.2	−22.8	−91.9
HSE06	−69.2	53.7	−104.6	−32.1	22.5	−8.8	−15.9	−86.7
LC-ωPBE	−89.6	80.0	−117.6	−51.5	49.5	−31.4	−8.1	−81.9
ωB97X-D	−54.5	49.7	−69.6	−22.6	21.6	−7.8	1.3	−60.3
cPKZB	−114.4	59.9	−166.4	−39.4	15.1	−14.4	0.6	−74.6
cTPSS	−90.4	62.4	−110.6	−33.3	14.4	−7.8	43.9	−40.2
cTPSSh	−75.7	58.0	−103.5	−32.6	18.0	−6.6	19.6	−63.1
cr^{2}SCAN	−131.8	90.0	−182.1	−56.9	34.9	−27.3	7.4	−94.3
cLH20t	−40.2	34.7	−59.2	−17.9	11.9	−0.7	−22.1	−70.3
Expt. (Chloroform)	−56	51.8	−78	−15.8	15.3	–	27.6	−41.1
Vaara *et al.* PBE0/NEVPT2	−65.1	53.6	−98.7	−28.4	22.1	−7.5	−12.0	−79.3
Liimatainen *et al.* B3LYP	−85.3	66.9	−117.9	−30.9	24.2	−14.6	26.8	−55.8

X2C-PBE0/x2c-QZVPall-s calculations lead to similar results as the PBE0/NEVPT2 ansatz, which demonstrates again that DFT is sufficient for the g-tensor and ZFS of this complex.

Considering the different density functional approximations, pure semilocal functionals are again outperformed by hybrids for most shifts. Notable exceptions in this regard are the shifts of H-27 and CH_3-1, where BP86 and PBE result in the best agreement with the experiment. However, both functionals perform rather inconsistent with large errors for H-10 and H-12. Therefore, the good agreement for H-27 and CH_3-1 is likely due to (partial) error cancellation. Overall, the range-separated hybrids CAM-B3LYP and ωB97X-D yield a reasonable agreement with the experimental data. The shifts of H-10, H-11, and H-12 are very well reproduced. Also, the shifts of H-26 and H-27 are in qualitative agreement. In contrast, the methyl group CH_3-1 is not correctly described. This may be partly attributed to the rather different HFC constants at the three hydrogens, i.e. −0.1938, 0.0732, and 0.1100 MHz. Hence, averaging the HFC contributions for comparison to the experiment in solution may lead to rather large errors.

Compared to the previous DFT approach by Liimatainen *et al.*[15] using the (now superseded) formulation of Pennanen and Vaara,[14] the B3LYP results using the correct expression of Soncini and Van den Heuvel[19] and a quadruple-ζ basis are an improvement for the shifts of H-10 to H-28. As discussed above, the results for the methyl groups are less reliable.

To illustrate the computational demands, calculations with all functionals except for LH20t take less than four hours (24 OpenMP threads of an Intel Xeon Gold 6212U CPU at 2.40 GHz) and the SCF procedure is the time-determining step. For PBE0, the SCF part takes two hours and the NMR steps need less than one hour. The situation changes for LH20t. Here, the SCF part amounts to about two hours, while the NMR part requires almost 4.5 hours. Therefore, LHFs are clearly computationally more demanding than conventional global or range-separated hybrids using seminumerical integration techniques, as previously discussed in ref. 41. For magnetic response properties, a multi-grid approach can be used for the conventional hybrids without loss of accuracy,[41,58,60,82,153] i.e. a large grid is used for the semilocal exchange-correlation parts and a small grid is used for the HF exchange terms. As LHF evaluate both the semilocal and HF exchange parts simultaneously, such a multi-grid approach is not straightforward and simply using a small grid for the left-hand side of the response equations results in serious convergence issues for the spin-flip part of the ZFS tensor.

Taking together, a fully consistent DFT framework and the DFT/MR hybrid approach lead to similar results for the quinolyl-functionalized cyclopentadienyl Cr(III) complex with a small ZFS contribution. A full DFT ansatz is clearly computationally cheaper and thus allows to use larger basis sets for routine calculations. In principle, this is advantageous for the HFC tensor which requires large basis sets for convergence.[43,59,189–191]

D. Three-Coordinate Mo(III) Complex: Mo[N(R)Ar]$_3$

The three-coordinate Mo(III) complex Mo[N(R)Ar]$_3$, displayed in Fig. 2 with the corresponding labels, serves as an example for large systems. With a quadruple-ζ basis set, this

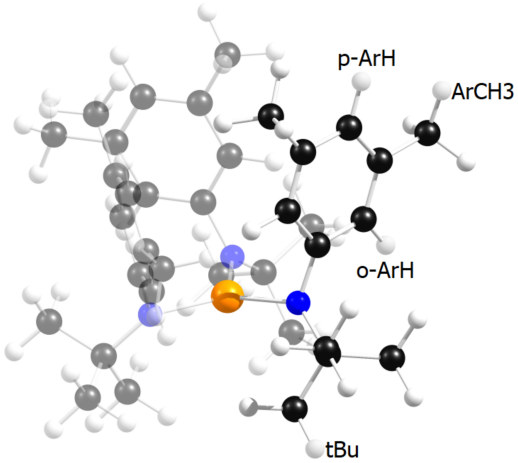

FIG. 2. Molecular structure of $Mo[N(R)Ar]_3$ with $S = 3/2$ and labels for the ^{1}H NMR. Color code: hydrogen white, carbon black, nitrogen blue, molybdenum orange. For simplicity, two of the three identical ligands are shown transparently for clarity. The structure was optimized at the BP86-D4/DLU-X2C/x2c-SVPall level in the present work. o-ArH and p-ArH refer to the ortho and para positions of the aryl group, respectively.

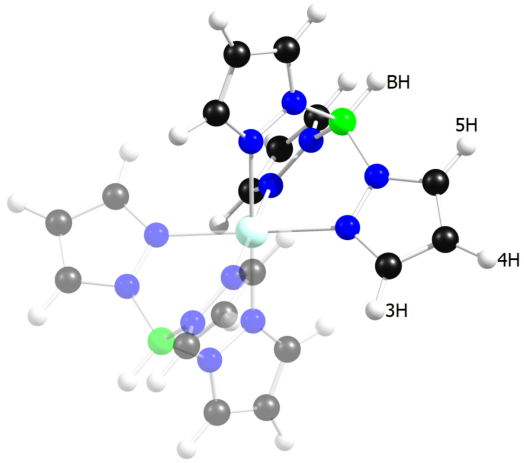

FIG. 3. Molecular structure of Co(II) pyrazolylborate complex HPYBCO with $S = 3/2$ and labels for the ^{1}H NMR. Color code: hydrogen white, boron magenta, carbon black, nitrogen blue, cobalt cyan. For simplicity, one of the two identical pyrazolborate ligands is shown transparently for clarity. The structure was taken from ref. 49.

TABLE VI. ^{1}H NMR chemical shifts (in ppm) of $Mo[N(R)Ar]_3$ with $S = 3/2$ at 298 K. See Fig. 2 for the labels of the hydrogens. Experimental data (Expt.) are taken from ref. 166. Individual contributions are listed in the Supporting Information (pNMR sheet in MoArComplex.xlsx). The ^{2}H (D) shift of the tBu group is 64.6 ppm.

Functional	tBu	o-ArH	$ArCH_3$	p-ArH
KT3	77.1	−68.9	−22.5	−80.8
BP86	80.7	−42.0	−18.0	−65.3
B3LYP	90.5	−44.6	−28.4	−65.0
CAM-B3LYP	89.6	−51.6	−39.3	−67.9
BH&HYLP	86.7	−89.4	−62.2	−99.4
PBE	87.0	−35.4	−15.3	−59.3
PBE0	77.7	−52.7	−33.7	−70.1
HSE06	79.9	−52.4	−33.9	−71.7
LC-ωPBE	70.7	−79.1	−58.6	−88.3
ωB97X-D	100.9	−47.0	−31.3	−60.9
cPKZB	83.0	−61.3	−17.7	−76.2
cTPSS	83.9	−48.9	−24.5	−62.5
cTPSSh	80.4	−54.9	−31.8	−67.1
cr^{2}SCAN	100.5	−79.0	−49.7	−103.4
cLH20t	87.5	−26.8	−17.7	−44.6
Expt. (Benzene)	64.0	ca. 23	−9.63	−51.67

compound features 5340 primitive and 4246 contracted basis functions in the spherical atomic orbital representation. Thus, DFT methods are desirable to perform routine calculations. For pure functionals, the complete pNMR shift calculation takes about 1.7 hours and hybrid functionals require 16.8 hours (24 OpenMP threads of an Intel Xeon Gold 6212U CPU at 2.40 GHz). Here, the SCF part is the time-determining step. The NMR results are shown in Tab. VI.

The NMR shift of the tBu group is in reasonable agreement with the experimental findings and the large downfield shift is reproduced. Similar findings hold for the large upfield shift of the $ArCH_3$ group. The p-ArH shift is also rather well reproduced. In contrast, the result for o-ArH is off. The paramagnetic shift is completely due to the FC part, as the PC term almost vanishes. The ZFS D parameter is within a range from -6 to $-14\,\mathrm{cm}^{-1}$ and the E/D ratio amounts to about 0.01. Thus, the ZFS contribution affects the shifts by only 0.5 ppm. As three of the four shifts are in qualitative agreement with the experiment, we do not expect that the ZFS and g-tensor are subject to pronounced multireference effects.

The three pure density functional approximations BP86, PBE, cTPSS, lead to similar results with PBE yielding slightly better results than BP86 or cTPSS. Hybrid functionals do not lead to a notable improvement. Among the hybrids, the local hybrid LH20t results in the smallest deviation for the hydrogen shifts of $ArCH_3$ and p-ArH. However, it does not improve upon PBE, while notably increasing the computational costs.

To sum up, the large upfield and downfield shifts of p-ArH and tBu are qualitatively reproduced and some functionals also reproduce the $ArCH_3$ shift, however, the o-ArH shift is completely off. In contrast to the previous sections, conventional hybrid functionals are no improvement and only the local hybrid LH20t does not lead to a deterioration compared to PBE.

E. Co(II) Complex HPYBCO

The Co(II) pyrazolylborate complex HPYBCO with $S = 3/2$, displayed in Fig. 3 is a very challenging systems for DFT methods, as its ZFS and g-tensor show pronounced multireference effects and consequently all pNMR shfits are completely off compared to the experiment.

All functionals considered herein lead to a ZFS D parameter of about -5 to $-10\,\mathrm{cm}^{-1}$, whereas CASSCF and

TABLE VII. ^{1}H NMR shifts (in ppm) of the Co(II) pyrazolylborate complex HPYBCO with $S = 3/2$ at 298 K. For the position of the hydrogens, see Fig. 3. ZFS and g-tensors are obtained at the NEVPT2/DKH2 level with the x2c-TZVPall/x2c-SVPall basis sets, while the orbital shielding and HFCs tensors are obtained at the DFT/DLU-X2C level with the x2c-QZVPall-s bases. COSMO is applied with the settings for chloroform. Shifts are given relative to tetramethylsilane, see Supporting Information (Co-Complex-HPYBCO.xlsx). Experimental data (Expt.) are taken from ref. 192. See also ref. 193. Additional computational results of Vaara *et al.* using PBE0/NEVPT2 are taken from ref. 23. The def2-TZVP basis is employed for the HFC and orbital shielding tensors with PBE0, while the def2-TZVP/def2-SVP basis sets are used for the ZFS and g-tensor with NEVPT2. The assigment of the shifts is based on our results.

Functional	3H	4H	5H	BH
KT3	−89.6	63.5	115.8	114.6
BP86	−75.0	61.4	113.6	122.7
B3LYP	−93.2	42.8	101.0	129.5
CAM-B3LYP	−97.0	35.8	96.4	132.4
BH&HLYP	−108.5	25.9	92.4	136.6
PBE	−75.7	62.6	115.2	124.0
PBE0	−98.2	39.3	97.9	131.5
HSE06	−97.3	39.7	98.2	130.8
LC-ωPBE	−91.2	34.7	94.3	131.5
ωB97X-D	−104.0	36.3	98.3	133.8
cPKZB	−84.0	55.9	108.4	121.2
cTPSS	−86.9	66.4	115.6	121.4
cTPSSh	−93.7	55.2	106.8	124.4
cr^{2}SCAN	−87.3	53.0	109.0	117.4
cLH20t	−111.3	34.8	98.8	142.6
Expt. (Chloroform)	−111.0	42	94.2	122.0
Vaara *et al.* PBE0/NEVPT2	−92.9	37.9	95.2	128.3

NEVPT2 lead to a D parameter of around $-110\,\mathrm{cm}^{-1}$. Likewise, the g-tensor is not well described as its off-diagonal elements are too small and the principal components with DFT severely disagree with results from NEVPT2. The eigenvalues of the g-tensor with DFT are all close to about 2.1, while CASSCF or NEVPT2 leads to three notably different eigenvalues of 1.5, 1.7, and 3.2. Interestingly, the isotropic g-value with DFT is in very good agreement with the respective NEVPT2 and CASSCF results, which is due to error cancellation. Overall, this leads to a serious underestimate of the pseudo-contact term and all ^{1}H NMR shifts are completely off compared to the experiment,[192] see Supporting Information and refs. 23,49. Thus, a hybrid framework using CASSCF or NEVPT2 for the ZFS and g-tensor is indispensable.

The ^{1}H NMR shifts are listed in Tab. VII. Here, semilocal functionals such as PBE and cTPSS notably overestimate the 4H and 5H shifts, while the 3H shift is typically underestimated (in absolute numbers). This changes when using hybrid functionals. Then, the 5H shifts are well described with PBE-based functionals and HSE06 or ωB97X-D. The 3H and 4H shifts are still the most demanding cases. Here, only PBE0, HSE06, LC-ωPBE, ωB97X-D, and cLH20t perform well. The latter performs excellently for 3H but shows a larger deviation for 4H. For the BH shift, the pure functionals BP86, cPKZB, and cTPSS yield excellent results, whereas the aforementioned hybrids overestimate the shift by around 8%. The local hybrid cLH20t shows an error of about 15% and consequently looses some ground.

The computation time of the DFT part is about 3.3 hours for the SCF procedure and 1.8 hours for the pNMR part (PBE0/x2c-QZVPall-s with 24 OpenMP threads of an Intel Xeon Gold 6212U CPU at 2.40 GHz). The wall time for the CASSCF/NEVPT2 calculations amounts to around 5.5 hours (OpenMPI with 16 processors, AMD EPYC 7702P). For a more direct comparison of the computational demands, we also carried out DFT calculations with the same basis set as done for CASSCF/NEVPT2. Then, the complete DFT calculation takes 0.1 hours with PBE and 0.9 hours with PBE0 (16 OpenMP threads of an Intel Xeon Gold 6212U CPU at 2.40 GHz). Note that the SCF procedure completely dominates the total wall time with this basis set combination, as it requires 107 SCF iterations for PBE and 348 for PBE0 with a superposition of atomic densities as initial guess. With extended Hückel theory for the SCF initial guess, we need 220 iterations for PBE and 289 for PBE0. The pNMR part only takes 2 and 8 minutes, respectively. Therefore, a hybrid DFT/MR framework is much more demanding than the DFT-only methodology and should only be used for systems with pronounced multireference character such as, e.g., open-shell Fe and Co complexes.

Overall, the PBE0, HSE06, and ωB97X-D perform well when using wavefunction-based multireference methods such as NEVPT2 for the ZFS and g-tensor. All shifts are reproduced within an error range of about 10% compared to the experiment. In contrast to the other systems studied herein, cobalt-based complexes mark a clear limitation for a DFT-only framework.

F. $Cp^*MoCl_3(PMePh_2)$ and $ReCl_3py_2(PPh_3)$

The complexes $Cp^*MoCl_3(PMePh_2)$ and $ReCl_3py_2(PPh_3)$ with $S = 1$ serve as additional examples for 4d and 5d transition metal complexes. First, we consider the calculated chemical shifts of $Cp^*MoCl_3(PMePh_2)$ displayed in Fig. 4. The NMR chemical shifts are listed in Tab. VIII. Here, we do not consider the shifts of the phenyl rings, as the experimental assignment was unclear and not fully discussed in the experimental reference,[169] which seriously hinders an analysis of the limitations of our proposed methodology. Therefore, averaged results for both of the phenyl rings are only listed in the Supporting Information (CpMo-Complex.xlsx).

Overall, we do not observe good agreement with experiment. With the exception of the Cp* shift caculated with cTPSSh, the ^{1}H NMR shifts of the Cp^* ring and of the PMe group deviate notably from the experimental values. For the Cp^* ring, the results depend strongly on the chosen functional. These deviations originate mostly from the FC contribution, as the PC contribution is always very close to zero.

In order to rule out the influence of a faulty description of the ZFS and g-tensor, both of these properties were calculated on the CASSCF(2,5)/NEVPT2 level, in a fashion

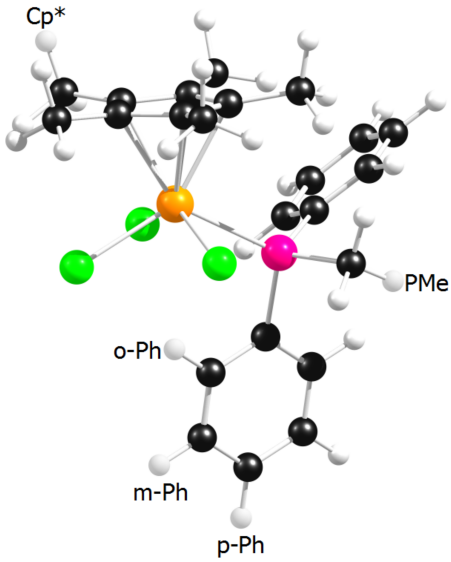

FIG. 4. Molecular structure of $Cp^*MoCl_3(PMePh_2)$ with $S = 1$ and labels for the ^{1}H NMR. Color code: hydrogen white, carbon black, phosphorus pink, chlorine green, molybdenum orange. The structure was optimized at the BP86-D4/DLU-X2C/x2c-TZVPall-s level herein.

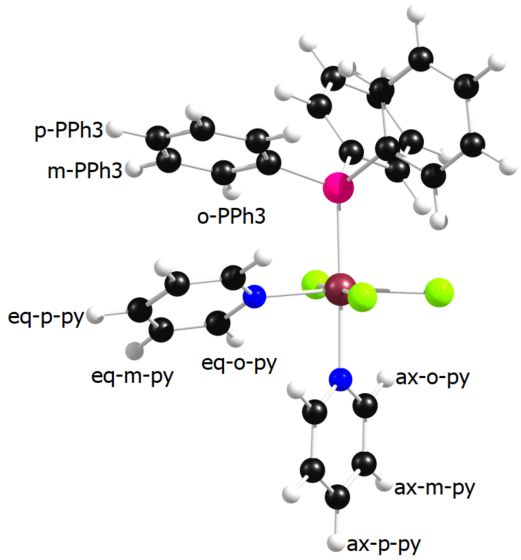

FIG. 5. Molecular structure of $ReCl_3py_2(PPh_3)$ with $S = 1$ and labels for the ^{1}H NMR. Color code: hydrogen white, carbon black, nitrogen blue, phosphorus pink, chlorine green, rhenium red. The structure was optimized at the BP86-D4/DLU-X2C/x2c-TZVPall-s level in the present work. o-PPh_3, m-PPh_3, p-PPh_3 refer to the ortho, meta, and para positions of the phenyl ligand. ax and eq denote axial and equatorial position, respectively.

TABLE VIII. ^{1}H NMR chemical shifts (in ppm) of $Cp^*MoCl_3(PMePh_2)$ at 298 K ($S = 1$) with various density functional approximations. For the labels of the hydrogens, see Fig. 4. Additionally, results from a PBE0/NEVPT2 hybrid framework are shown. Experimental data (Expt.) are taken from ref. 169. Individual contributions are listed in the Supporting Information (CpMo-Complex.xlsx).

Method	Cp^*	PMe
BP86	4.13	−36.36
B3LYP	−7.48	−36.55
CAM-B3LYP	−17.86	−39.23
PBE	7.85	−35.17
PBE0	−19.78	−43.72
ωB97X-D	−12.67	−36.22
cTPSSh	−0.39	−38.05
PBE0/NEVPT2	−19.29	−42.59
Expt. (Acetone)	−2.5	−13.4

similar to the one proposed in ref. 49. Both g_{iso} and the D parameter are in good agreement with the PBE0 results (PBE0: $g_{iso} = 1.984$, $D = 2.29\,cm^{-1}$, CASSCF/NEVPT2: $g_{iso} = 1.938$, $D = 2.79\,cm^{-1}$). The actual tensors can be found in the respective input files for the PNMRshift program in the Supporting Information. Due to this good agreement, using the CASSCF/NEVPT2 tensors does not change the chemical shifts significantly, as shown in Tab. VIII. Therefore, it is plausible, that the problem really lies in a faulty description of the HFC tensors.

Investigating the actual isotropic HFC constants of the Cp^* ring, which are listed in the Supporting Information (HFC_detailed sheet in CpMo-Complex.xlsx), it becomes evident that the constants are often rather small. Size and sign of the constants are unevenly distributed among the 15 equivalent atoms. Comparing the functionals, the differences in the descriptions of the individual atoms lead to different averages over the 15 atoms, which results in the observed deviating predictions of the chemical shifts. Here, the determination of the chemical shift seems to be rather unreliable.

For the PMe group, all functionals produce a Fermi-contact shift with the correct sign but with too large of an absolute value, resulting in the large negative total chemical shifts. These large calculated FC shifts can mostly be attributed to one of the three H atoms, with a negative HFC constant of more than −1.3 MHz for all considered functionals (in absolute numbers). Here, it seems that the HFC constant on one of the atoms dominates the overall result and its absolute HFC constant is probably overestimated.

Therefore, in both considered cases, there seems to be a problem with the accurate description of the HFC constants of the H atoms. This likely corresponds to some extent to an inaccurate description of the spin-excess density on these atoms.

Second, we consider the $ReCl_3py_2(PPh_3)$ complex shown in Fig. 5. Here, the experimental values for the pyridine ligands (py) were just assigned to the o-, m- and p-positions, but not to the axial (ax) or equatorial (eq) position, which is why two values are listed for the three corresponding pyridine shifts. As evident from the results in Tab. IX, the shifts of the PPh_3 ligands are in good agreement with the experiment. In contrast, the shifts on the pyridine ligands are not well described by our method. Here, the PC shift often points in the

TABLE IX. ^{1}H NMR chemical shifts (in ppm) of $ReCl_3py_2(PPh_3)$ at 298 K ($S = 1$) with various density functional approximations. Additionally, results from a PBE0/NEVPT2 hybrid framework are shown. For the labels of the hydrogens, see Fig. 5. Experimental data (Expt.) are taken from ref. 170. Individual contributions are listed in the Supporting Information (Re-Complex.xlsx). Here, the experimental values for the pyridine ligands (py) were just assigned to the o-, m- and p-positions, but not to the axial (ax) or equatorial (eq) position. Thus, two values are listed for the three corresponding pyridine shifts.

Method	o-PPh_3	m-PPh_3	p-PPh_3	ax-o-py	eq-o-py	ax-m-py	eq-m-py	ax-p-py	eq-p-py
BP86	21.85	11.99	11.48	22.59	−2.01	28.73	25.65	13.09	17.42
B3LYP	20.89	10.75	11.17	22.79	−3.18	29.19	20.03	10.18	13.69
CAM-B3LYP	21.46	10.20	11.44	17.83	−14.08	33.39	17.57	7.61	6.90
PBE	22.14	12.16	11.34	24.32	−0.72	28.24	25.61	13.32	16.43
PBE0	22.24	10.42	12.22	19.72	−1.76	30.72	19.54	8.87	17.89
ωB97X-D	21.81	10.21	11.53	21.17	−12.24	31.65	16.01	9.19	8.56
cTPSSh	22.62	11.63	11.59	20.93	1.33	30.49	24.97	8.61	16.71
PBE0/NEVPT2	14.87	8.94	9.57	11.32	2.00	16.92	11.87	9.27	11.65
Expt. (Chloroform)	18.06	10.09	10.88	(-58.59, -76.53)		(34.17, 37.18)		(-46.88, -77.66)	

wrong direction, resulting in the wrong sign for the total shift. Only for the m-py part, the sign of the shifts is correctly reproduced and the shifts are in the right order of magnitude.

As for $Cp^*MoCl_3(PMePh_2)$, we tried to narrow down the root of the problem by carrying out CASSCF(4,5)/NEVPT2 calculations of the ZFS and g-tensor. Here, the results deviate strongly from the PBE0 results (PBE0: $g_{iso} = 2.158$, $D = 717.02\,cm^{-1}$, CASSCF/NEVPT2: $g_{iso} = 1.942$, $D = 1815.74\,cm^{-1}$). Accordingly, using the CASSCF/NEVPT2 tensors for the PNMRshift program leads to notably different chemical shifts with respect to PBE0. However, the pyridine shifts are still completely off, as shown in Tab. IX.

Assuming an accurate description with the multireference approach for the ZFS and g-tensor, the problem again seems to stem from the HFC tensor. In contrast to $Cp^*MoCl_3(PMePh_2)$, the problem cannot be narrowed down to the isotropic constant of the HFC tensor, as it may also be due to the anisotropic contribution (mainly the SD term).

To conclude, tests on these two Mo and Re complexes, which were experimentally studied,[169,170] demonstrate a clear limitation of the presented method. This can at least in parts be attributed to inaccurately described HFC tensors on some H atoms within the DFT framework, which in turn points to some extent to inaccuracies in the description of the spin-excess density. Note that this limitation also affects the DFT/MR hybrid framework, which makes use of DFT for the HFC tensor. Here, MR methods for the HFC tensor such as that outlined in refs. 194–196 may be beneficial.

IV. CONCLUSION

We presented an efficient and fully consistent DFT-based approach up to the class of current-dependent local hybrid functionals for the calculation of paramagnetic NMR shifts within scalar-relativistic X2C theory augmented by spin–orbit perturbation theory. The efficiency of this ansatz allows us to use large basis sets for the description of the HFC tensors to compute the pNMR shifts with EPR tensors. Throughout this work, we consider a broad range of density functional approximations. For metallocenes, it was demonstrated that this approach can generally yield a very good agreement for ^{1}H shifts with experiment—especially if hybrid functionals such as PBE0 and ωB97X-D are employed. In addition, X2C-DFT calculations on a quinolyl-functionalized cyclopentadienyl Cr(III) complex showed similar results to a reported DFT/MR hybrid approach,[23] where the ZFS and g-tensor are calculated with NEVPT2. Severe limitations for the DFT-only approach were observed for the Co(II) complex HPYBCO, as here both the ZFS and the g-tensor are completely off with respect to NEVPT2 results, which was already described in the literature based on the PBE and PBE0 functionals.[49] Here, a DFT/MR hybrid approach is mandatory to obtain reasonable chemical shifts. For Co, this is not unexpected, as Co complexes with more than one unpaired electron are among the well known multireference problems.[49] Generally, meta-GGAs and local hybrids or other modern functionals are no systematic improvement upon GGAs and conventional hybrids. Thus, PBE, PBE0, and ωB97X-D are still a very reasonable choice for initial studies.

Possible issues with the description of the ZFS and g-tensor are not the only limitations of the presented ansatz. Poor agreement with experimental ^{1}H shifts was obtained for some hydrogens of $Cp^*MoCl_3(PMePh_2)$ and $ReCl_3py_2(PPh_3)$. These results could not be improved by calculating the ZFS and g-tensors at the NEVPT2 level. Here, the problem seems to originate from an insufficient description of the HFC tensors of some H atoms. Therefore, the HFC tensor at the ligand atoms is not always correctly reproduced by DFT methods and the currently available functionals, which in turn leads to wrong paramagnetic shifts. This means that even within one molecule a good description of some of the pNMR shifts does not necessarily make the other predicted shifts reliable, as shown for the three-coordinate Mo(III) complex $Mo[N(tBu)Ar]_3$. This affects all frameworks making use of DFT for the HFC tensor and clearly shows that there is still room for improvement concerning density functional approximations for pNMR shifts and the HFC tensor.

Generally, we recommend the following workflow. First a DFT calculation with a large basis set (QZVP) together with

the PBE, PBE0, and ωB97X-D is carried out to check if reasonable results are obtained. The large basis is used to ensure that the HFC tensors are converged with respect to the basis set. If there is very poor agreement with the obtained shifts, a NEVPT2 approach for the calculation of the ZFS and g-tensor should be considered, as described in, e.g., Ref. 49. However, this might not lead to improvements for all considered shifts as well. Then, a potential solution would be to also use multireference methods for the HFC tensor. This would necessitate the use of large basis sets for all atoms, at which the HFC tensors of interest are centered, and likely an expansion of the active space beyond the orbitals on the central atom, at which the spin-excess density is mainly located. Thus, this would lead to substantially increased computational costs.

SUPPLEMENTARY MATERIAL

Supporting Information is available with the structures optimized in this work (txt file), complete data (zip archive with xlsx files), and input files for the PNMRShift program (zip archive with text files in ASCII format).

ACKNOWLEDGMENTS

The authors thank Karin Fink (KIT) for helpful discussions regarding the CASSCF/NEVPT2 calculations. We gratefully acknowledge support from the Deutsche Forschungsgemeinschaft (DFG, German Research Foundation) through the Collaborative Research Centre "4f for Future" (CRC 1573 project no. 471424360, project Q) Y.J.F. acknowledges financial support by Turbomole GmbH. S.G. is supported by a fellowship from Fonds der Chemischen Industrie (FCI no. 110160, German Chemical Industry Funds). C.H. gratefully acknowledges funding by the Volkswagen Foundation.

DATA AVAILABILITY STATEMENT

The data that support the findings of this study are available within the article and its supplementary material.

AUTHOR CONTRIBUTIONS

Yannick J. Franzke: Conceptualization (equal); Data Curation (equal); Formal Analysis (equal); Investigation (equal); Methodology (equal); Software (lead); Supervision (supporting); Validation (equal); Visualization (supporting); Writing - Original Draft (equal); Writing - Review & Editing (equal). **Florian Bruder**: Conceptualization (equal); Data Curation (equal); Formal Analysis (equal); Investigation (equal); Methodology (equal); Software (supporting); Validation (equal); Writing - Original Draft (equal); Writing - Review & Editing (equal). **Sebastian Gillhuber**: Conceptualization (supporting); Formal Analysis (supporting); Investigation (supporting); Methodology (equal); Visualization (lead); Writing - Review & Editing (supporting). **Christof Holzer**: Conceptualization (supporting); Formal Analysis (supporting); Investigation (supporting); Methodology (equal); Writing - Review & Editing (supporting). **Florian Weigend**: Conceptualization (supporting); Formal Analysis (supporting); Investigation (supporting); Methodology (equal); Supervision (lead); Writing - Review & Editing (supporting).

CONFLICT OF INTEREST

The authors have no conflicts to disclose.

REFERENCES

[1] J. Vaara, Phys. Chem. Chem. Phys. **9**, 5399 (2007).
[2] M. Kaupp, M. Bühl, and V. G. Malkin, eds., *Calculation of NMR and EPR Parameters. Theory and Applications* (Wiley-VCH, Weinheim, Germany, 2004).
[3] J. Autschbach, J. Chem. Phys. **136**, 150902 (2012).
[4] J. Autschbach, Philos. Trans. A Math. Phys. Eng. Sci. **372**, 20120489 (2014).
[5] I. Bertini, C. Luchinat, and G. Parigi, *Solution NMR of Paramagnetic Molecules*, Vol. 2 (Elsevier, Amsterdam, The Netherlands, 2001).
[6] C. P. Grey and N. Dupré, Chem. Rev. **104**, 4493 (2004).
[7] M. Kaupp and F. H. Köhler, Coord. Chem. Rev. **253**, 2376 (2009).
[8] P. H. Keizers and M. Ubbink, Prog. Nucl. Magn. Reson. Spectrosc. **58**, 88 (2011).
[9] A. J. Pell, G. Pintacuda, and C. P. Grey, Prog. Nucl. Magn. Reson. Spectrosc. **111**, 1 (2019).
[10] H. M. McConnell and R. E. Robertson, J. Chem. Phys. **29**, 1361 (1958).
[11] R. J. Kurland and B. R. McGarvey, J. Magn. Reson. **2**, 286 (1970).
[12] Z. Rinkevicius, J. Vaara, L. Telyatnyk, and O. Vahtras, J. Chem. Phys. **118**, 2550 (2003).
[13] S. Moon and S. Patchkovskii, "First-Principles Calculations of Paramagnetic NMR Shifts," in *Calculation of NMR and EPR Parameters*, edited by M. Kaupp, M. Bühl, and V. G. Malkin (Wiley-VCH, Weinheim, Germany, 2004) Chap. 20, pp. 325–338.
[14] T. O. Pennanen and J. Vaara, Phys. Rev. Lett. **100**, 133002 (2008).
[15] H. Liimatainen, T. O. Pennanen, and J. Vaara, Can. J. Chem. **87**, 954 (2009).
[16] I. Bertini, C. Luchinat, and G. Parigi, Prog. Nucl. Magn. Reson. Spectrosc. **40**, 249 (2002).
[17] W. Van den Heuvel and A. Soncini, Phys. Rev. Lett. **109**, 073001 (2012).
[18] W. Van den Heuvel and A. Soncini, J. Chem. Phys. **138**, 054113 (2013).
[19] A. Soncini and W. Van den Heuvel, J. Chem. Phys. **138**, 021103 (2013).
[20] F. Gendron, K. Sharkas, and J. Autschbach, J. Phys. Chem. Lett. **6**, 2183 (2015).
[21] B. Martin and J. Autschbach, J. Chem. Phys. **142**, 054108 (2015).
[22] B. Martin and J. Autschbach, J. Chem. Phys. **145**, 049901 (2016).
[23] J. Vaara, S. A. Rouf, and J. Mareš, J. Chem. Theory Comput. **11**, 4840 (2015).
[24] S. Komorovský, M. Repiský, K. Ruud, O. L. Malkina, and V. G. Malkin, J. Phys. Chem. A **117**, 14209 (2013).
[25] T. Helgaker, M. Jaszuński, and K. Ruud, Chem Rev. **99**, 293 (1999).
[26] J. Autschbach, S. Patchkovskii, and B. Pritchard, J. Chem. Theory Comput. **7**, 2175 (2011).
[27] E. van Lenthe, E. J. Baerends, and J. G. Snijders, J. Phys. Chem. **99**, 4597 (1993).
[28] E. van Lenthe, E. J. Baerends, and J. G. Snijders, J. Chem. Phys. **101**, 9783 (1994).
[29] J. Autschbach and B. Pritchard, Theor. Chem. Acc. **129**, 453 (2011).
[30] G. te Velde, F. M. Bickelhaupt, E. J. Baerends, C. Fonseca Guerra, S. J. A. van Gisbergen, J. G. Snijders, and T. Ziegler, J. Comput. Chem. **22**, 931 (2001).

[31] F. Neese, F. Wennmohs, U. Becker, and C. Riplinger, J. Chem. Phys. **152**, 224108 (2020).
[32] B. Martin and J. Autschbach, Phys. Chem. Chem. Phys. **18**, 21051 (2016).
[33] M. R. Pederson and S. N. Khanna, Phys. Rev. B **60**, 9566 (1999).
[34] F. Neese, J. Chem. Phys. **127**, 164112 (2007).
[35] S. Schmitt, P. Jost, and C. van Wüllen, J. Chem. Phys. **134**, 194113 (2011).
[36] Manual of ADF 2023.1, see `https://www.scm.com/doc/ADF/Input/ESREPR.html` (retrieved September 19, 2023).
[37] G. L. Stoychev, A. A. Auer, R. Izsák, and F. Neese, J. Chem. Theory Comput. **14**, 619 (2018).
[38] D. Flaig, M. Maurer, M. Hanni, K. Braunger, L. Kick, M. Thubauville, and C. Ochsenfeld, J. Chem. Theory Comput. **10**, 572 (2014).
[39] S. Lehtola, M. Dimitrova, H. Fliegl, and D. Sundholm, J. Chem. Theory Comput. **17**, 1457 (2021).
[40] S. Lehtola, M. Dimitrova, H. Fliegl, and D. Sundholm, J. Chem. Theory Comput. **17**, 4629 (2021).
[41] C. Holzer, Y. J. Franzke, and M. Kehry, J. Chem. Theory Comput. **17**, 2928 (2021).
[42] J. B. Stückrath, T. Gasevic, M. Bursch, and S. Grimme, Inorg. Chem. **61**, 3903 (2022).
[43] Y. J. Franzke and J. M. Yu, J. Chem. Theory Comput. **18**, 323 (2022).
[44] Y. J. Franzke and J. M. Yu, J. Chem. Theory Comput. **18**, 2246 (2022).
[45] S. Gohr, P. Hrobárik, M. Repiský, S. Komorovský, K. Ruud, and M. Kaupp, J. Phys. Chem. A **119**, 12892 (2015).
[46] A. M. Teale, O. B. Lutnæs, T. Helgaker, D. J. Tozer, and J. Gauss, J. Chem. Phys. **138**, 024111 (2013).
[47] Z. W. Windom, A. Perera, and R. J. Bartlett, J. Chem. Phys. **156**, 094107 (2022).
[48] M. Glasbrenner, S. Vogler, and C. Ochsenfeld, J. Chem. Phys. **148**, 214101 (2018).
[49] S. A. Rouf, J. Mareš, and J. Vaara, J. Chem. Theory Comput. **11**, 1683 (2015).
[50] M. Douglas and N. M. Kroll, Ann. Phys. (NY) **82**, 89 (1974).
[51] B. A. Hess, Phys. Rev. A **33**, 3742 (1986).
[52] G. Jansen and B. A. Hess, Phys. Rev. A **39**, 6016 (1989).
[53] E. Malkin, M. Repiský, S. Komorovský, P. Mach, O. L. Malkina, and V. G. Malkin, J. Chem. Phys. **134**, 044111 (2011).
[54] M. Repisky, S. Komorovsky, M. Kadek, L. Konecny, U. Ekström, E. Malkin, M. Kaupp, K. Ruud, O. L. Malkina, and V. G. Malkin, J. Chem. Phys. **152**, 184101 (2020).
[55] S. A. Rouf, J. Mareš, and J. Vaara, J. Chem. Theory Comput. **13**, 3731 (2017).
[56] A. Pyykkönen, R. Feher, F. H. Köhler, and J. Vaara, Inorg. Chem. **59**, 9294 (2020).
[57] A. Pyykkönen and J. Vaara, Phys. Chem. Chem. Phys. **25**, 3121 (2023).
[58] F. Bruder, Y. J. Franzke, C. Holzer, and F. Weigend, ChemRxiv (2023), 10.26434/chemrxiv-2023-2kh59-v2, preprint.
[59] S. Gillhuber, Y. J. Franzke, and F. Weigend, J. Phys. Chem. A **125**, 9707 (2021).
[60] F. Bruder, Y. J. Franzke, and F. Weigend, J. Phys. Chem. A **126**, 5050 (2022).
[61] W. Kutzelnigg and W. Liu, J. Chem. Phys. **123**, 241102 (2005).
[62] W. Liu and W. Kutzelnigg, J. Chem. Phys. **126**, 114107 (2007).
[63] W. Liu and D. Peng, J. Chem. Phys. **125**, 044102 (2006).
[64] W. Liu and D. Peng, J. Chem. Phys. **125**, 149901 (2006).
[65] M. Iliaš and T. Saue, J. Chem. Phys. **126**, 064102 (2007).
[66] W. Liu and D. Peng, J. Chem. Phys. **131**, 031104 (2009).
[67] D. Peng, W. Liu, Y. Xiao, and L. Cheng, J. Chem. Phys. **127**, 104106 (2007).
[68] K. G. Dyall, J. Chem. Phys. **106**, 9618 (1997).
[69] K. G. Dyall, J. Chem. Phys. **109**, 4201 (1998).
[70] K. G. Dyall and T. Enevoldsen, J. Chem. Phys. **111**, 10000 (1999).
[71] K. G. Dyall, J. Chem. Phys. **115**, 9136 (2001).
[72] C. Holzer, Y. J. Franzke, and A. Pausch, J. Chem. Phys. **157**, 204102 (2022).
[73] Y. J. Franzke and F. Weigend, J. Chem. Theory Comput. **15**, 1028 (2019).
[74] J. Jaramillo, G. E. Scuseria, and M. Ernzerhof, J. Chem. Phys. **118**, 1068 (2003).
[75] J. F. Dobson, J. Chem. Phys. **98**, 8870 (1993).
[76] A. D. Becke, J. Chem. Phys. **117**, 6935 (2002).
[77] J. Tao, Phys. Rev. B **71**, 205107 (2005).
[78] C. J. Schattenberg and M. Kaupp, J. Chem. Theory Comput. **17**, 1469 (2021).
[79] Y. J. Franzke, C. Holzer, and F. Mack, J. Chem. Theory Comput. **18**, 1030 (2022).
[80] Y. J. Franzke and C. Holzer, J. Chem. Phys. **157**, 031102 (2022).
[81] Y. J. Franzke, F. Mack, and F. Weigend, J. Chem. Theory Comput. **17**, 3974 (2021).
[82] Y. J. Franzke, J. Chem. Theory Comput. **19**, 2010 (2023).
[83] N. Mardirossian and M. Head-Gordon, Mol. Phys. **115**, 2315 (2017).
[84] N. Mardirossian and M. Head-Gordon, J. Chem. Theory Comput. **12**, 4303 (2016).
[85] P. Hao, J. Sun, B. Xiao, A. Ruzsinszky, G. I. Csonka, J. Tao, S. Glindmeyer, and J. P. Perdew, J. Chem. Theory Comput. **9**, 355 (2013).
[86] L. Goerigk, A. Hansen, C. Bauer, S. Ehrlich, A. Najibi, and S. Grimme, Phys. Chem. Chem. Phys. **19**, 32184 (2017).
[87] G. Vignale and M. Rasolt, Phys. Rev. Lett. **59**, 2360 (1987).
[88] J. E. Bates and F. Furche, J. Chem. Phys. **137**, 164105 (2012).
[89] A. D. Becke, Phys. Rev. A **38**, 3098 (1988).
[90] J. P. Perdew, Phys. Rev. B **33**, 8822 (1986).
[91] O. Treutler, *Entwicklung und Anwendung von Dichtefunktionalmethoden*, Dissertation (Dr. rer. nat.), University of Karlsruhe (TH), Germany (1995).
[92] O. Treutler and R. Ahlrichs, J. Chem. Phys. **102**, 346 (1995).
[93] Y. J. Franzke, R. Treß, T. M. Pazdera, and F. Weigend, Phys. Chem. Chem. Phys. **21**, 16658 (2019).
[94] E. Caldeweyher, S. Ehlert, A. Hansen, H. Neugebauer, S. Spicher, C. Bannwarth, and S. Grimme, J. Chem. Phys. **150**, 154122 (2019).
[95] D. Peng, N. Middendorf, F. Weigend, and M. Reiher, J. Chem. Phys. **138**, 184105 (2013).
[96] Y. J. Franzke, N. Middendorf, and F. Weigend, J. Chem. Phys. **148**, 104410 (2018).
[97] D. Peng and M. Reiher, J. Chem. Phys. **136**, 244108 (2012).
[98] Y. J. Franzke, L. Spiske, P. Pollak, and F. Weigend, J. Chem. Theory Comput. **16**, 5658 (2020).
[99] L. Visscher and K. G. Dyall, At. Data Nucl. Data Tables **67**, 207 (1997).
[100] P. Pollak and F. Weigend, J. Chem. Theory Comput. **13**, 3696 (2017).
[101] K. Reiter, F. Mack, and F. Weigend, J. Chem.Theory Comput. **14**, 191 (2018).
[102] T. W. Keal and D. J. Tozer, J. Chem. Phys. **119**, 3015 (2003).
[103] T. W. Keal and D. J. Tozer, J. Chem. Phys. **121**, 5654 (2004).
[104] J. P. Perdew, K. Burke, and M. Ernzerhof, Phys. Rev. Lett. **77**, 3865 (1996).
[105] C. Adamo and V. Barone, J. Chem. Phys. **110**, 6158 (1999).
[106] C. Lee, W. Yang, and R. G. Parr, Phys. Rev. B **37**, 785 (1988).
[107] A. D. Becke, J. Chem. Phys. **98**, 1372 (1993).
[108] P. J. Stephens, F. J. Devlin, C. F. Chabalowski, and M. J. Frisch, J. Phys. Chem. **98**, 11623 (1994).
[109] T. Yanai, D. P. Tew, and N. C. Handy, Chem. Phys. Lett. **393**, 51 (2004).
[110] Y. Jin and R. J. Bartlett, J. Chem. Phys. **145**, 034107 (2016).
[111] R. L. A. Haiduke and R. J. Bartlett, J. Chem. Phys. **149**, 131101 (2018).
[112] J. Heyd, G. E. Scuseria, and M. Ernzerhof, J. Chem. Phys. **118**, 8207 (2003).
[113] J. Heyd, G. E. Scuseria, and M. Ernzerhof, J. Phys. Chem. **124**, 219906 (2006).
[114] A. V. Krukau, O. A. Vydrov, A. F. Izmaylov, and G. E. Scuseria, J. Phys. Chem. **125**, 224106 (2006).
[115] O. A. Vydrov and G. E. Scuseria, J. Chem. Phys. **125**, 234109 (2006).
[116] J.-D. Chai and M. Head-Gordon, Phys. Chem. Chem. Phys. **10**, 6615 (2008).
[117] J. Tao, J. P. Perdew, V. N. Staroverov, and G. E. Scuseria, Phys. Rev. Lett. **91**, 146401 (2003).
[118] V. N. Staroverov, G. E. Scuseria, J. Tao, and J. P. Perdew, J. Chem. Phys. **119**, 12129 (2003).
[119] S. Grimme, J. Phys. Chem. A **109**, 3067 (2005).
[120] J. W. Furness, A. D. Kaplan, J. Ning, J. P. Perdew, and J. Sun, J. Phys. Chem. Lett. **11**, 8208 (2020).
[121] J. W. Furness, A. D. Kaplan, J. Ning, J. P. Perdew, and J. Sun, J. Phys. Chem. Lett. **11**, 9248 (2020).
[122] M. Bursch, H. Neugebauer, S. Ehlert, and S. Grimme, J. Chem. Phys. **156**, 134105 (2022).

[123] J. Tao and Y. Mo, Phys. Rev. Lett. **117**, 073001 (2016).
[124] Y. Zhao and D. G. Truhlar, J. Chem. Phys. **125**, 194101 (2006).
[125] R. Peverati and D. G. Truhlar, J. Phys. Chem. Lett. **3**, 117 (2012).
[126] R. Peverati and D. G. Truhlar, Phys. Chem. Chem. Phys. **14**, 13171 (2012).
[127] H. S. Yu, X. He, and D. G. Truhlar, J. Chem. Theory Comput. **12**, 1280 (2016).
[128] H. S. Yu, X. He, S. L. Li, and D. G. Truhlar, Chem. Sci. **7**, 5032 (2016).
[129] J. P. Perdew, S. Kurth, A. c. v. Zupan, and P. Blaha, Phys. Rev. Lett. **82**, 2544 (1999).
[130] A. D. Boese and J. M. L. Martin, J. Chem. Phys. **121**, 3405 (2004).
[131] N. Mardirossian and M. Head-Gordon, J. Chem. Phys. **142**, 074111 (2015).
[132] N. Mardirossian and M. Head-Gordon, J. Chem. Phys. **144**, 214110 (2016).
[133] T. Aschebrock and S. Kümmel, Phys. Rev. Res. **1**, 033082 (2019).
[134] A. V. Arbuznikov and M. Kaupp, J. Chem. Phys. **136**, 014111 (2012).
[135] M. Haasler, T. M. Maier, R. Grotjahn, S. Gückel, A. V. Arbuznikov, and M. Kaupp, J. Chem. Theory Comput. **16**, 5645 (2020).
[136] C. Holzer and Y. J. Franzke, J. Chem. Phys. **157**, 034108 (2022).
[137] E. R. Johnson, J. Chem. Phys. **141**, 124120 (2014).
[138] J. P. Perdew, V. N. Staroverov, J. Tao, and G. E. Scuseria, Phys. Rev. A **78**, 052513 (2008).
[139] M. A. L. Marques, M. J. T. Oliveira, and T. Burnus, Comput. Phys. Commun. **183**, 2272 (2012).
[140] S. Lehtola, C. Steigemann, M. J. T. Oliveira, and M. A. L. Marques, SoftwareX **7**, 1 (2018).
[141] "Libxc," Version 6.2.2, available from `https://www.tddft.org/programs/libxc/` (retrieved July 26, 2023).
[142] A. Schäfer, A. Klamt, D. Sattel, J. C. W. Lohrenz, and F. Eckert, Phys. Chem. Chem. Phys. **2**, 2187 (2000).
[143] C. Holzer, J. Chem. Phys. **153**, 184115 (2020).
[144] P. Plessow and F. Weigend, J. Comput. Chem. **33**, 810 (2012).
[145] H. Bahmann and M. Kaupp, J. Chem. Theory Comput. **11**, 1540 (2015).
[146] C. J. Schattenberg, K. Reiter, F. Weigend, and M. Kaupp, J. Chem. Theory Comput. **16**, 931 (2020).
[147] F. Furche, B. T. Krull, B. D. Nguyen, and J. Kwon, J. Chem. Phys. **144**, 174105 (2016).
[148] M. Kehry, Y. J. Franzke, C. Holzer, and W. Klopper, Mol. Phys. **118**, e1755064 (2020).
[149] M. Filatov, W. Zou, and D. Cremer, J. Chem. Phys. **139**, 014106 (2013).
[150] W. Zou, M. Filatov, and D. Cremer, J. Chem. Phys. **142**, 214106 (2015).
[151] T. Yoshizawa, W. Zou, and D. Cremer, J. Chem. Phys. **145**, 184104 (2016).
[152] M. Häser, R. Ahlrichs, H. P. Baron, P. Weis, and H. Horn, Theor. Chim. Acta **83**, 455 (1992).
[153] Y. J. Franzke and C. Holzer, J. Chem. Phys. (2023), 10.1063/5.0171509, in press.
[154] TURBOMOLE GmbH, (2023), developers' version of TURBOMOLE V7.7.1, a development of University of Karlsruhe and Forschungszentrum Karlsruhe GmbH, 1989-2007, TURBOMOLE GmbH, since 2007; available from `https://www.turbomole.org` (retrieved July 26, 2023).
[155] R. Ahlrichs, M. Bär, M. Häser, H. Horn, and C. Kölmel, Chem. Phys. Lett. **162**, 165 (1989).
[156] S. G. Balasubramani, G. P. Chen, S. Coriani, M. Diedenhofen, M. S. Frank, Y. J. Franzke, F. Furche, R. Grotjahn, M. E. Harding, C. Hättig, A. Hellweg, B. Helmich-Paris, C. Holzer, U. Huniar, M. Kaupp, A. Marefat Khah, S. Karbalaei Khani, T. Müller, F. Mack, B. D. Nguyen, S. M. Parker, E. Perlt, D. Rappoport, K. Reiter, S. Roy, M. Rückert, G. Schmitz, M. Sierka, E. Tapavicza, D. P. Tew, C. van Wüllen, V. K. Voora, F. Weigend, A. Wodyński, and J. M. Yu, J. Chem. Phys. **152**, 184107 (2020).
[157] Y. J. Franzke, C. Holzer, J. H. Andersen, T. Begušić, F. Bruder, S. Coriani, F. Della Sala, E. Fabiano, D. A. Fedotov, S. Fürst, S. Gillhuber, R. Grotjahn, M. Kaupp, M. Kehry, M. Krstić, F. Mack, S. Majumdar, B. D. Nguyen, S. M. Parker, F. Pauly, A. Pausch, E. Perlt, G. S. Phun, A. Rajabi, D. Rappoport, B. Samal, T. Schrader, M. Sharma, E. Tapavicza, R. S. Treß, V. Voora, A. Wodyński, J. M. Yu, B. Zerulla, F. Furche, C. Hättig, M. Sierka, D. P. Tew, and F. Weigend, J. Chem. Theory Comput. (2023), 10.1021/acs.jctc.3c00347.
[158] B. Pritchard, B. Martin, and J. Autschbach, (2022), PNMRShift Program (git commit dc2b8c5), see `https://github.com/jautschbach/pnmr-shift/tree/master` (retrieved September 19, 2023).
[159] F. London, J. Phys. Radium **8**, 397 (1937).
[160] R. Ditchfield, Mol. Phys. **27**, 789 (1974).
[161] N. Hebendanz, F. H. Koehler, G. Mueller, and J. Riede, J. Am. Chem. Soc. **108**, 3281 (1986).
[162] N. Hebendanz, F. H. Köhler, F. Scherbaum, and B. Schlesinger, Magn. Reson. Chem. **27**, 798 (1989).
[163] A. Jaworski and N. Hedin, Phys. Chem. Chem. Phys. **24**, 15230 (2022).
[164] F. Weigend and R. Ahlrichs, Phys. Chem. Chem. Phys. **7**, 3297 (2005).
[165] P. Fernández, H. Pritzkow, J. J. Carbó, P. Hofmann, and M. Enders, Organometallics **26**, 4402 (2007).
[166] C. E. Laplaza, M. J. A. Johnson, J. C. Peters, A. L. Odom, E. Kim, C. C. Cummins, G. N. George, and I. J. Pickering, J. Am. Chem. Soc. **118**, 8623 (1996).
[167] F. Neese, WIREs Comput. Mol. Sci. **12**, e1606 (2022).
[168] F. Neese, "ORCA – an ab initio, density functional and semiempirical program package, V. 5.0.4, MPI für Kohlenforschung, Mülheim a. d. Ruhr (Germany)," (2023), available from `https://orcaforum.kofo.mpg.de/` (retrieved October 17, 2023).
[169] F. Abugideiri, J. C. Gordon, R. Poli, B. E. Owens-Waltermire, and A. L. Rheingold, Organometallics **12**, 1575 (1993).
[170] C. Pearson and A. L. Beauchamp, Can. J. Chem. **75**, 220 (1997).
[171] R. Prins, J. van Voorst, and C. Schinkel, Chem. Phys. Lett. **1**, 54 (1967).
[172] P. Baltzer, A. Furrer, J. Hulliger, and A. Stebler, Inorg. Chem. **27**, 1543 (1988).
[173] S. Li, Y. M. Hamrick, R. J. Van Zee, and W. J. Weltner, J. Am. Chem. Soc. **114**, 4433 (1992).
[174] M. F. Rettig and R. S. Drago, J. Am. Chem. Soc. **91**, 1361 (1969).
[175] F. Neese, J. Chem. Phys. **122**, 034107 (2005).
[176] F. Neese, J. Am. Chem. Soc. **128**, 10213 (2006).
[177] S. Lehtola and M. A. L. Marques, J. Chem. Phys. **157**, 174114 (2022).
[178] S. Lehtola, J. Phys. Chem. A **127**, 4180 (2023).
[179] S. Lehtola, J. Chem. Theory Comput. **19**, 2502 (2023).
[180] E. König, R. Schnakig, B. Kanellakopulos, and R. Klenze, Chem. Phys. Lett. **50**, 439 (1977).
[181] T. H. Dunning, J. Chem. Phys. **90**, 1007 (1989).
[182] N. B. Balabanov and K. A. Peterson, J. Chem. Phys. **123**, 064107 (2005).
[183] W. Kutzelnigg, U. Fleischer, and M. Schindler, in *Deuterium and Shift Calculation* (Springer, Berlin, Heidelberg, Germany, 1991) pp. 165–262.
[184] T. Noro, M. Sekiya, and T. Koga, Theor. Chem. Acc. **131**, 1124 (2012).
[185] K. G. Dyall, Theor. Chem. Acc. **115**, 441 (2006).
[186] T. Saue, R. Bast, A. S. P. Gomes, H. J. A. Jensen, L. Visscher, I. A. Aucar, R. Di Remigio, K. G. Dyall, E. Eliav, E. Fasshauer, T. Fleig, L. Halbert, E. D. Hedegård, B. Helmich-Paris, M. Iliaš, C. R. Jacob, S. Knecht, J. K. Laerdahl, M. L. Vidal, M. K. Nayak, M. Olejniczak, J. M. H. Olsen, M. Pernpointner, B. Senjean, A. Shee, A. Sunaga, and J. N. P. van Stralen, J. Chem. Phys. **152**, 204104 (2020).
[187] R. Bast, A. S. P. Gomes, T. Saue, L. Visscher, H. J. A. Jensen, I. A. Aucar, V. Bakken, C. Chibueze, J. Creutzberg, K. G. Dyall, S. Dubillard, U. Ekström, E. Eliav, T. Enevoldsen, E. Faßhauer, T. Fleig, O. Fossgaard, L. Halbert, E. D. Hedegård, T. Helgaker, B. Helmich-Paris, J. Henriksson, M. van Horn, M. Iliaš, C. R. Jacob, S. Knecht, S. Komorovský, O. Kullie, J. K. Lærdahl, C. V. Larsen, Y. S. Lee, N. H. List, H. S. Nataraj, M. K. Nayak, P. Norman, A. Nyvang, G. Olejniczak, J. Olsen, J. M. H. Olsen, A. Papadopoulos, Y. C. Park, J. K. Pedersen, M. Pernpointner, J. V. Pototschnig, R. Di Remigio Eikås, M. Repiský, K. Ruud, P. Sałek, B. Schimmelpfennig, B. Senjean, A. Shee, J. Sikkema, A. Sunaga, J. Thyssen, J. van Stralen, M. L. Vidal, S. Villaume, O. Visser, T. Winther, S. Yamamoto, and X. Yuan, "DIRAC23," (2023), available from Zendo, `https://doi.org/10.5281/zenodo.7670749`.
[188] F. Jensen, J. Chem. Theory Comput. **11**, 132 (2015).
[189] P. Jakobsen and F. Jensen, J. Chem. Phys. **151**, 174107 (2019).
[190] E. D. Hedegård, J. Kongsted, and S. P. A. Sauer, J. Chem. Theory Comput. **7**, 4077 (2011).
[191] A. R. Al Derzi, S. Fau, and R. J. Bartlett, J. Phys. Chem. A **107**, 6656 (2003).
[192] K. Długopolska, T. Ruman, M. Danilczuk, and D. Pogocki, Appl. Magn. Reson. **35**, 271 (2009).
[193] W. K. Myers, E. N. Duesler, and D. L. Tierney, Inorg. Chem. **47**, 6701 (2008).

[194]R. Feng, T. J. Duignan, and J. Autschbach, J. Chem. Theory Comput. **17**, 255 (2021).

[195]L. Birnoschi and N. F. Chilton, J. Chem. Theory Comput. **18**, 4719 (2022).

[196]T. Bodenstein, A. Heimermann, K. Fink, and C. van Wüllen, ChemPhysChem **23**, e202100648 (2022).